Anomalous spin dynamics and excitations of the quasizigzag chain compound $AgCrP_2S_6$

Hyun-gi Lee,[1] Changhyun Koo,[1,*] Youngsu Choi,[1] Yugo Oshima,[2] Rajesh Kumar Ulaganathan,[3] Raju Kalaivanan,[4] Raman Sankar,[4,†] and Kwang-Yong Choi[1,‡]

[1]*Department of Physics, Sungkyunkwan University, Suwon 16419, Republic of Korea*
[2]*RIKEN Cluster for Pioneering Research, Wako, Saitama 351-0198, Japan*
[3]*Centre for Nanotechnology, Indian Institute of Technology Roorkee, 247667, India*
[4]*Institute of Physics, Academia Sinica, Nankang, Taipei 11529, Taiwan*

(Received 4 February 2025; accepted 25 March 2025; published 10 April 2025)

We investigate the spin dynamics and low-energy magnetic excitations of an $S = 3/2$ spin zigzag chain system in the van der Waals material $AgCrP_2S_6$ using electron spin resonance (ESR) and Raman spectroscopy. The temperature-dependent resonance intensity and g factor reveal the development of critical correlations as the temperature approaches the ordering temperature. Additionally, the temperature-dependent linewidth of the magnetic resonance exhibits power-law behavior, characteristic of low-dimensional spin systems. The twofold angular dependence of the ESR linewidth and the significant magnetic Raman scattering in interchain (bb) polarization suggests coupling between the zigzag Cr^{3+} chains. Furthermore, anomalies in the ESR parameters and the Fano mode observed in Raman data around $T^* \approx 120$ K, together with an order-parameter-like shift of the magnetic spectral weight toward T^*, indicate a change in the nature of the underlying magnetic excitations, induced by non-negligible next-nearest neighbor interactions and interchain couplings, which become effective below T^*.

DOI: 10.1103/PhysRevB.111.134415

I. INTRODUCTION

van der Waals (vdW) materials have garnered extensive interest in both engineering and fundamental research due to their unique layered structures, which underpin exceptional electrical, optical, thermodynamic, magnetic, and mechanical characteristics [1–9]. The distinct atomic arrangement of these materials features covalent bonding within individual layers, while adjacent layers are connected by weaker vdW interactions. This structural framework facilitates the embodiment of two-dimensional (2D) systems, as exemplified by exfoliated graphene, rendering vdW materials a foundational platform for multifunctional and hybrid devices [10].

Among vdW materials, transition-metal dichalcogenides (TMDs) have been extensively studied for their sizable band gaps, which distinguish them from gapless materials like graphene. These properties position TMDs as promising candidates for applications in switching and optoelectronic devices [11,12]. This is particularly significant in the context of the Mermin-Wagner theorem [13], which precludes magnetic ordering in isotropic 2D magnetic systems. Recent studies, however, demonstrate that vdW materials with magnetic anisotropy can support magnetic long-range order in the 2D limit [14–16], paving the way for investigating intriguing magnetic behaviors and quantum phenomena.

The capacity to control dimensionality in vdW materials adds another compelling aspect to their study [17]. For instance, honeycomb antiferromagnets MPS_3 (M = transition metal) exhibit various 2D magnetic configurations such as alternating antiferromagnetic (AFM), Néel-type AFM, and zigzag-type AFM states [18]. Substituting magnetic M sites with nonmagnetic atoms, as in $AgCrP_2S_6$, disrupts the original magnetic interactions, creating zigzag Cr chains separated by nonmagnetic Ag chains [18]. These 1D frustrated magnets, characterized by competing nearest-neighbor (NN) interactions J_1 and next-nearest neighbor (NNN) interactions J_2 enable exploration of the 1D $S = 1/2$ zigzag chain model and associated dimensional reduction. Depending on the ratio $\alpha = J_1/J_2$, diverse magnetic phases are predicted [19–22]. For example, when $\alpha = 0$, the zigzag chains effectively decouple into two independent AFM chains. For $\alpha > 0$ with antiferromagnetic J_1, a gapped dimerized phase transitions into a critical gapless phase at $\alpha \approx 4.15$. Conversely, for $\alpha < 0$ with ferromagnetic J_1, an incommensurate spin-spin correlation phase transits into a ferromagnetic gapless phase emerging at $\alpha = -4$. As the spin quantum number increases beyond $S = 1/2$, the system undergoes a transition from gapless quantum phases toward more classical behavior [23].

$AgCrP_2S_6$ (Cr^{3+}, $S = 3/2$) is a noteworthy vdW material for delving into dimensionality reduction and 1D zigzag spin chain dynamics. This material exhibits a platelike, layered morphology with a space group of $P2/a$ [18]. As illustrated in Figs. 1(a) and 1(b) inset, Ag and Cr atoms occupy a honeycomb lattice, separated by S and P atoms, which form alternating zigzag chains along the crystal a axis. Consequently, the Cr chains can be effectively modeled as 1D

*Contact author: chkoo@skku.edu
†Contact author: sankarndf@gmail.com
‡Contact author: choisky99@skku.edu

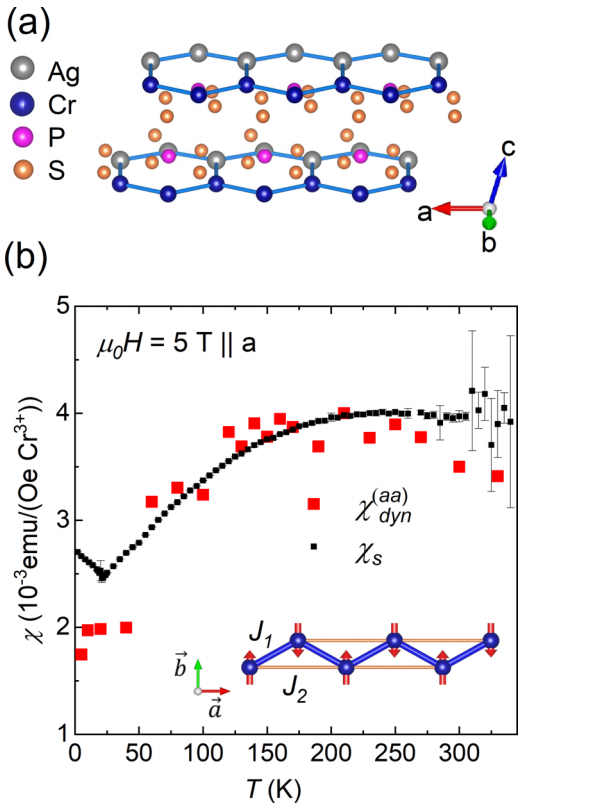

FIG. 1. (a) Layered crystal structure of $AgCrP_2S_6$. The gray, blue, pink, and orange spheres represent Ag, Cr, P, and S atoms, respectively. The layered honeycomb networks of Ag^+ and Cr^{3+} ions are separated by P and S atoms. (b) Temperature dependence of the magnetic susceptibility of $AgCrP_2S_6$ measured at $\mu_0 H = 5\,\mathrm{T}||a$, plotted together with the dynamic Raman susceptibility (red squares) derived from the magnetic Raman response in the (*aa*) scattering configuration. The inset sketches $S = 3/2$ zigzag spin chains of magnetic Cr^{3+} ions along the a axis within the honeycomb layers. The thick and thin solid lines denote the nearest-neighbor J_1 and next-nearest neighbor J_2 exchange interactions, respectively.

zigzag chains with weak interchain interactions. Magnetic susceptibility measurements indicate strong AFM intrachain interactions of -100 K [24]. On the other hand, density functional theory (DFT) calculations suggest an AFM zigzag rung interaction of $J_1 = -45.33$ K and a ferromagnetic (FM) ladder-leg interaction of $J_2 = 6.72$ K within the exchange interaction form of $-JS_iS_{i+1}$ [17]. The long-range magnetic ordering occurs at $T_N = 21$ K, as inferred from powder neutron diffraction and magnetic susceptibility data [17,25]. Inelastic neutron-scattering experiments probe a continuum of excited states above the ordering temperature, suggesting the quantum flucutations characteristic of 1D spin chains in this material [26,27]. However, the absence of a complete mapping of the magnetic excitation spectra leaves their precise nature unresolved. Given that the $S = 3/2$ zigzag spin chains lie at the crossover between quantum and classical behavior, a detailed study of spin dynamics and magnetic excitations is sought.

In this study, we investigate single crystals of $AgCrP_2S_6$ using magnetic susceptibility, *X*-band electron spin resonance (ESR), and Raman spectroscopy. We identify a characteristic temperature, $T^* \sim 120$ K, at which magnetic Raman scattering, Fano phonon behavior, and ESR parameters undergo distinct changes. These findings offer fresh insights into the interplay between dimensionality, frustration, and magnetic correlations in $S = 3/2$ zigzag spin chains.

II. METHODS

A. Crystal growth

Single crystals of $AgCrP_2S_6$ were grown using the chemical vapor transport method. All chemical preparations were carried out in an argon-filled glovebox. The starting materials Ag_2S, Cr, P, and S were mixed in a molar ratio of 1:2:4:11 using an agate mortar. The mixture was sealed in a quartz ampoule of dimensions $20 \times 16 \times 250$ mm^3 under a vacuum of 3×10^{-3} mbar. The ampoule was placed in a tube furnace. Initially, the furnace was uniformly heated to 400 °C at a rate of 100 °C/h and held for 24 h to stabilize the reaction. It was then further heated to 700 °C at the same rate. The reaction region was maintained at 700 °C for 510.5 h. Subsequently, the sink region was heated to 750 °C at 100 °C/h, held for 24 hand then cooled back to 700 °C at a slow rate of 1 °C/h. To further facilitate crystal growth, the sink region was gradually cooled to 650 °C at a rate of 0.5 °C/h and kept at this temperature for 336 h. Finally, the source region was cooled to room temperature at a faster rate of 50 °C/h. We obtained shiny black crystals with typical dimensions of 5 mm × 2 mm × 100 μm.

B. Magnetic susceptibility

Magnetic susceptibility measurements were performed using a superconducting quantum interference device magnetometer (Quantum Design MPMS). The static magnetic susceptibility data were collected for a magnetic field of $\mu_0 H = 5$ T applied parallel to the a axis over a temperature range of $T = 2$–340 K.

C. Raman spectroscopy

Raman-scattering experiments were performed in backscattering geometry using a micro-Raman spectrometer (XperRam200VN, NanoBase) equipped with an air-cooled charge-coupled device detector. A 532-nm laser (DPSS SLM) with a power $P = 200$ mW was focused onto the sample with a ∼1-μm spot size. A Bragg-grade notch filter was employed to eliminate stray light, enabling Raman signal detection down to $\sim 10\,\mathrm{cm}^{-1}$. Temperature-dependent measurements were performed by varying the sample temperature between 5 and 390 K in a liquid helium-cooled continuous-flow cryostat.

D. Electron spin resonance

ESR measurements were carried out with a conventional *X*-band ($f = 9.12$ GHz) ESR spectrometer (JEOL, JES-RE3X) at RIKEN. The modulation amplitude, frequency, and microwave power used for ESR measurements were 2.0 mT, 100 kHz, and 4 mW, respectively. A single crystal (approximately $0.1 \times 1.5 \times 3.5\,\mathrm{mm}^3$) of $AgCrP_2S_6$ was loaded on a quartz rod, allowing the magnetic field to apply parallel and perpendicular to the

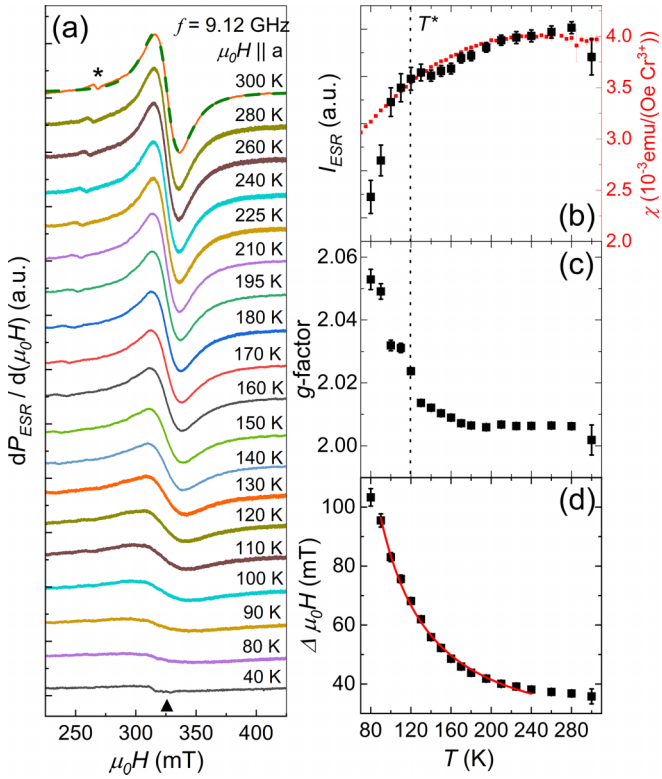

FIG. 2. (a) ESR spectra recorded at various temperatures at $f = 9.12$ GHz for an external magnetic field parallel to the a axis. The dashed line overlaid on the spectrum at $T = 300$ K represents the fitting using a derivative Lorentzian function. The asterisk indicates a small feature in the low magnetic field and the triangle indicates an experimental artifact. All spectra are offset for clarity. Temperature dependence of (b) the integrated intensity, (c) the g factor, and (d) the peak-to-peak linewidth obtained from the fittings of the ESR spectra shown in (a). The red data points in (b) are the susceptibility data from Fig. 1(b). The vertical dotted line marks a characteristic temperature $T^* = 120$ K. The red solid line in (d) represents the fitting curve obtained using a power-law function. See the text for the detail of the fitting.

a axis. A continuous ^{4}He-flow cryostat enabled controlling temperatures for the experiments from 3.7 to 300 K.

III. RESULTS AND DISCUSSION

A. Magnetic susceptibility and electron spin resonance

To confirm the sample quality, we first examined the magnetic susceptibility. As exhibited in Fig. 1(b), the magnetic susceptibility measured for $\mu_0 H = 5\,\mathrm{T}||a$ showed a broad maximum over a wide temperature range of $T = 150$–340 K, followed by its gradual supression. Eventually, the cusp minimum at $T_\mathrm{N} = 21$ K suggested the onset of long-range AFM order, consistent with previous studies [17,25].

We next elucidated the spin dynamics inherent to the $S = 3/2$ zigzag spin chain system by measuring ESR spectra. Figure 2(a) presents the derivatives of the ESR absorption lines recorded at various temperatures while applying a magnetic field along the a axis. A single Lorentzian absorption was observed down to about 80 K. Below this temperature, the ESR resonance signal became too weak to detect, mainly due to the development of critical magnetic correlations near the magnetic ordering temperature, which resulted in the wipeout of the ESR signal within the GHz time window. Below T_N, the AFM resonance signal may be also undetectable due to the presence of sizable magnon gaps exceeding the 9.12-GHz frequency. Additionally, a background signal with experimental artifact, marked by a triangle symbol in the spectrum at 40 K, hindered spectra analysis in this temperature range. Thus, the ESR analysis was limited to the temperatures above 80 K.

In addition to the main resonance signal, a small feature, indicated with an asterisk in Fig. 2(a), was observed in the low magnetic field range with $g = 2.45$ at $T = 300$ K. As the temperature decreased, this feature shifted to lower fields and eventually became indistinguishable below 120 K. Although the small feature showed temperature-dependent behavior similar to the main signal, its presence was unusual in a material containing Cr^{3+} ions at such high temperatures. While the origin of the small feature is currently unclear, it may arise from surface signals.

Next, the ESR parameters were attained by fitting the ESR signals using a derivative of a Lorentzian line profile, as exemplified by the representative fit at $T = 300$ K in the dashed line of Fig. 2(a). The resulting integrated intensity, g factor, and peak-to-peak linewidth of the ESR absorption lines are plotted in Figs. 2(b), 2(c), and 2(d), respectively. For temperatures above 100 K, the integrated intensity followed a similar trend as the static magnetic susceptibility [the red data points in Fig. 2(b)], showing a gradual increase up to 300 K. Below 100 K, the integrated ESR intensity decreased abruptly. This deviation from the static magnetic susceptibility was attributed to the development of antiferromagnetic critical correlations, which progressively wiped out the spins participating in the magnetic resonance as T_N was approached. At $T = 300$ K, the determined g factor of $g = 2.00(5)$ was close to the expected value of $g = 2.00$, typical for a less than half-filled Cr^{3+} ion with negligible spin-orbit interaction. This g factor remained largely temperature independent down to 200 K, followed by a notable increase with further decreasing temperatures below 200 K. This temperature roughly coincided with the maximum in the magnetic susceptibility. As such, the shift in the g factor was linked to the development of short-range magnetic correlations.

On the other hand, as the temperature decreased from 300 K, the ESR linewidth initially evolved slowly and then showed a sharp increase, signaling the critical slowing down of spin fluctuations upon approaching T_N. This critical-like broadening was described by a power-law dependence $(T - T_\mathrm{N})^p + c$, with $p = -1.4(1)$ and $c = 22(3)$ at $T_\mathrm{N} = 21$ K. The observed power-law broadening over a wide temperature range, on the one order of J, is a hallmark of low-dimensional spin systems, where pronounced quantum fluctuations and critical spin correlations are dominant. Due to a significant wipeout effect, the linewidth became indeterminable for temperatures below 80 K.

We next turn to the angular variation of the ESR linewidth to gain insights into the dimensionality of spin systems, anisotropy, the magnitude of spin interactions, and spin diffusion. Figure 3 displays the angular dependence of the ESR linewidth at 280 K, measured as a function of the angle

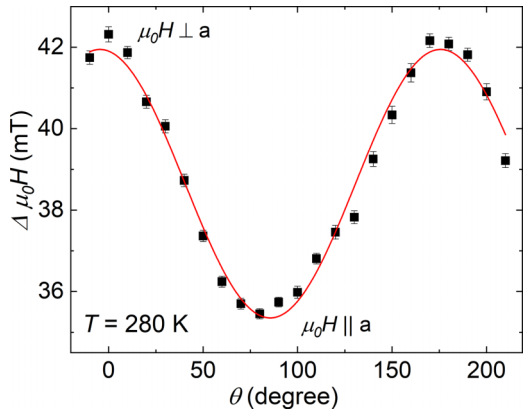

FIG. 3. Angle-dependent linewidth of the resonances at $T = 280$ K. The angle values are offset in consideration of the crystal orientation. The red solid line represents the fitting of the data using the function $\cos^2(\theta) + 1$.

between the external magnetic field and the a axis. The linewidth reaches a maximum when the external magnetic field is perpendicular to the a axis, and a minimum when the magnetic field is parallel to the a axis. A narrower linewidth indicates stronger spin interactions in the corresponding orientation [28], $\Delta\mu_0 H \cong 1/J$, consistent with the experimental geometry, where spin-exchange interactions primarily occur along the chain direction, a axis. The angle-dependent linewidth data were fitted using the function $\cos^2(\theta) + 1$ with a π interval, revealing a typical twofold anisotropy in the compound.

In a strict 1D system, however, the angle-dependent linewidth is expected to exhibit a W-like shape, $[3\cos^2(\theta) - 1]^2$, due to anisotropic spin diffusion along different directions. This characteristic behavior is commonly observed in ESR studies of 1D systems [29–31]. The deviation of our data from this expected angle-dependent behavior suggests that the magnetism of $AgCrP_2S_6$ cannot be captured within a strict spin chain model.

B. Raman spectroscopy

We now turn our attention to low-lying magnetic excitations probed through double spin-flip Raman-scattering processes. Figures 4(a)–4(c) compare the $T = 5$ K Raman spectra of $AgCrP_2S_6$ in the (aa), (ab), and (bb) scattering symmetries.

Based on factor group analysis for the space group *P2/a*, we expected 30 irreducible Raman-active phonon modes, given by $\Gamma = 14A_g$ (aa, bb) $+ 16B_g$ (ab). In the frequency range of 20–680 cm^{-1}, we observed all anticipated $14A_g$ modes in parallel polarizations, while $14B_g$ modes were identified in cross polarization. The lacking modes were likely due to either weak phonon intensity or their overlap with other phonons. In addition to one-phonon excitations, we also observed a dozen two-phonon scatterings superimposed on top of the broad magnetic background [color shadings in Figs. 4(a) and 4(c)], extending up to 1600 cm^{-1}.

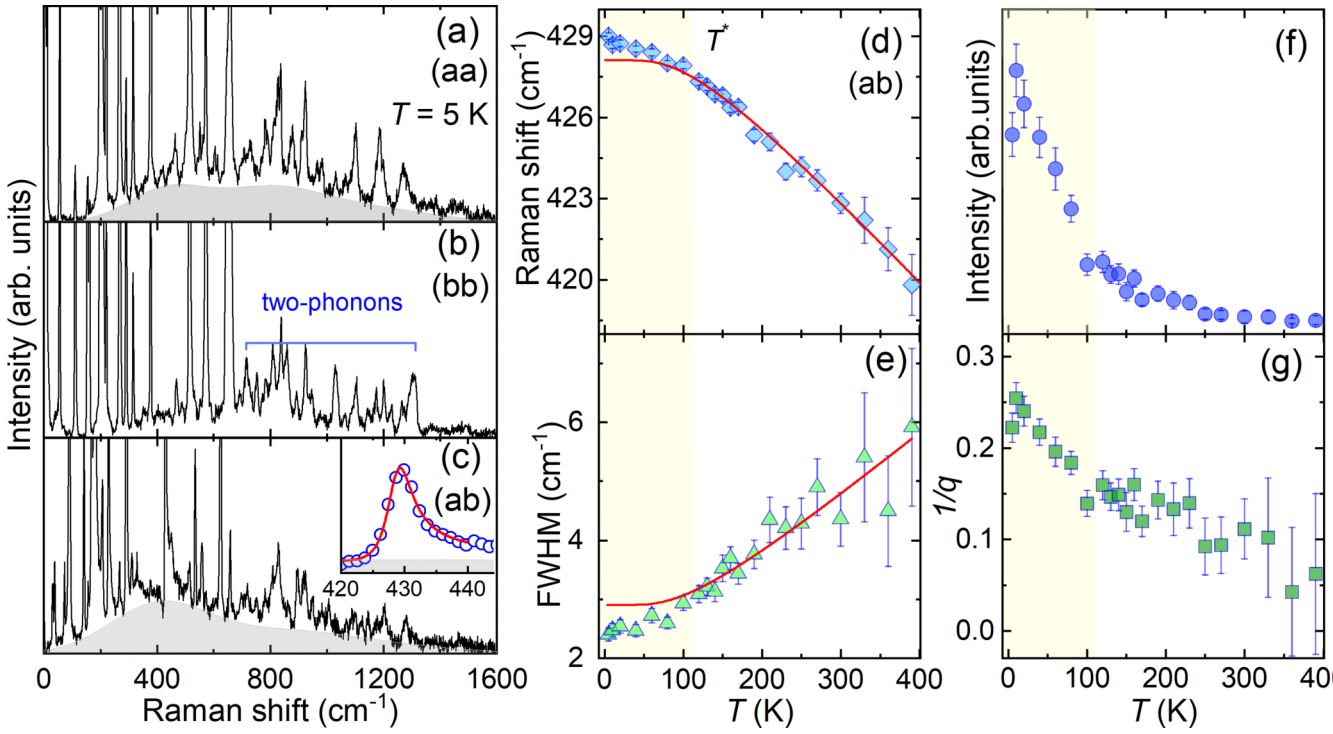

FIG. 4. (a)–(c) Polarization-resolved Raman spectra measured in (aa), (bb), and (ab) polarizations at $T = 5$ K. The inset of (c) depicts the Fano phonon peak at 429 cm^{-1}. Red solid line in the inset represents the fitting to the Fano mode. See the text for the detail of the fitting. Temperature dependence of (d) the energy, (e) linewidth, (f) intensity, and (g) Fano asymmetry $1/|q|$, with fittings based on the anharmonic phonon model fitting (red solid lines). The vertical shaded regions denote the temperature ranges where anomalies in the Fano phonon are observed.

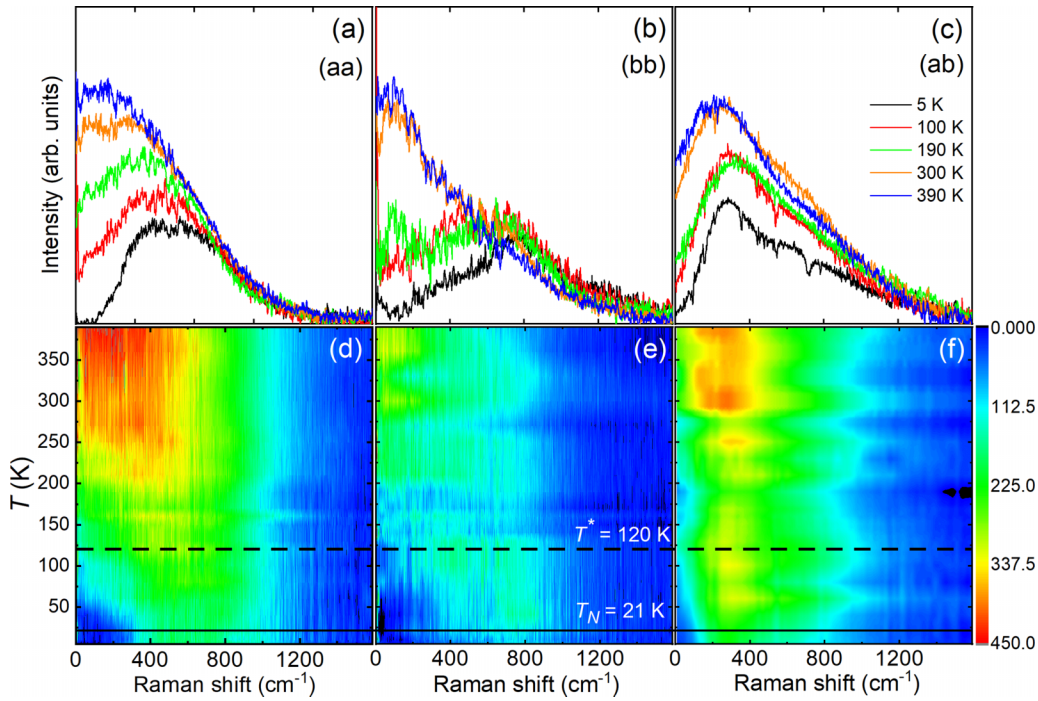

FIG. 5. (a)–(c) Temperature and polarization dependence of magnetic Raman spectra in (*aa*), (*bb*), and (*ab*) polarization configurations. (d)–(f) Color plots of the magnetic Raman intensity in the T-ω plane. The horizontal dashed lines denote the antiferromagnetic ordering temperature T_N and the characteristic temperature T^* associated with the energy scale of J.

Notably, the existence of a magnetic continuum is further hinted at by the observation of a Fano resonance at 429 cm^{-1} [see the inset of Fig. 4(c)]. The Fano profile is given by $I(\omega) = I_0(q+\varepsilon)^2/(1+\varepsilon^2)$, where the reduced energy is defined as $\varepsilon = (\omega-\omega_0)/\Gamma$. Here, ω_0 represents the bare phonon frequency, Γ is the linewidth, and q characterizes the Fano asymmetry. The fitting parameters for the Fano profile are plotted in Figs. 4(d)–4(g) as a function of temperature. Similarly, the frequency and linewidth of the Fano phonon mode deviated from the anharmonic phonon model [32] for temperatures below $T^* = 120$ K. This anomaly suggested that the Fano phonon energy and lifetime were additionally affected by its coupling to magnetic excitations. We further recalled that the ESR parameters exhibited anomalies in the similar temperature T^*. As the temperature was lowered from 390 K, on the other hand, the intensity of the Fano mode gradually increased down to T^*, followed by a steep rise. Similarly, the Fano asymmetry, $1/|q|$, increased continuously from 0.06 to 0.14 in the temperature range between T^* and 390 K and then underwent a rapid increase to 0.26 upon further cooling. Overall, the observed anomaly in the Fano resonance alluded to a change in the nature of the underlying magnetic excitation as our compound passed through T^*.

We next turn to magnetic Ramana scattering, which arises from double spin-flip processes from a ground state ($S = 3/2$, $S_z = \pm 3/2$) to an excited state ($S = 3/2$, $S_z = \pm 1/2$), while conserving a total spin $\Delta S_z = 0$. The spectral shape and polarization dependence of the Raman scattering intensity $I_R(\omega)$ convey information about the nature of quasiparticle excitations and the underlying spin lattice. This is mainly based on the fact that the exchange-scattering mechanism, leading to magnetic Raman scattering, is described by the Fleury-Loudon operator $R = \sum_{\langle i,j\rangle}(\varepsilon_i \cdot \hat{r}_{ij})(\varepsilon_s \cdot \hat{r}_{ij}) S_i \cdot S_j$, where ε_i and ε_s are the polarization vectors of the incident and scattered light and $\hat{r}_{ij}$ is the unit vector connecting the sites i and j. As such, $I_R(\omega)$ involves the square of exchange interactions between nearest neighbors along the polarization direction.

In Figs. 5(a)–5(c), we present presentative magnetic excitations in three distinct polarizations: (ε_i, ε_s) = (*aa*), (*bb*), and (*ab*), after subtracting phonon peaks [32–36]. Remarkably, the magnetic continuum is anisotropic in its intensity, shape, and thermal evolution between the polarization configurations.

In intrachain (*aa*) polarization, we observed a broad, strong continuum extending up to 1600 cm^{-1}. This was contrasted by a weaker magnetic signal with the triangle-like shape in interchain (*bb*) polarization and a moderate magnetic continuum with an asymmetric line shape toward the lower energy in (*ab*) polarization. For the case of pure 1D spin chain, magnetic light scattering vanished in both (*bb*) and (*ab*) polarizations due to the lacking interchain interactions [37,38]. In this vein, the non-negligible $I_R(\omega)$ in (*bb*) polarization suggests that zigzag spin chains are coupled. This supports the conclusion drawn from the angle-dependent ESR linewidth.

Figures 5(d)–5(f) exhibits color contour plots of the magnetic scattering intensity in the $T-\omega$ plane after subtracting the sharp phonon peaks. Overall, the temperature evolution of the magnetic excitations revealed little change in their energy and lifetime across T_N. This observation suggested that conventional thermal behavior of magnons was insufficient to capture this phenomenon.

In (*aa*) and (*bb*) polarizations, the magnetic continuum gradually softened to lower frequencies, while the lower-energy part evolved to a notable quasielastic scattering around the temperature scale of J. On the other hand, in (*ab*) polarization, the peak position of the continuum excitations was largely retained, although a quasielastic response was systematically enhanced with increasing temperature up to 390 K. The disparate polarization dependence of the magnetic continuum, in conjunction with variations in its line shape, highlighted the possibility that the underlying nature of magnetic quasiparticles differed between directions parallel and perpendicular to the zigzag spin direction. Similar behavior has been reported in the coupled two-leg ladder compound Ba_2CuTeO_6 [39], which lies near a quantum-critical point from a magnetically ordered side. Further, polarization-resolved Raman scattering of the anisotropic triangular antiferromagnet $Ca_3ReO_5Cl_2$ showed a pronounced angular dependence of spinon and triplon excitations [40]. In particular, frustration-induced dimensional reduction was inferred from the thermal evolution of spinon and triplon excitations. Noteworthy is that an inelastic neutron-scattering study of $CsVCl_3$ revealed unusual magnetic excitations that deviated significantly from classical spin-wave behavior [41]. The magnetic spectrum was dominated by a dispersionless mode of strong intensity, while the conventional acoustic spin-wave branch exhibited only weak spectral intensity. This unusual intensity distribution may account for the absence of spin-wave-like dynamics in the thermal evolution of the magnetic Raman continuum as localized magnetic excitations remain robust against thermal fluctuations.

Last, we calculated the temperature dependence of the dynamic Raman susceptibility $\chi_{\rm dyn}^{(aa)}$ by integrating a Raman conductivity $\chi''(\omega)/\omega$ over the frequency range of $\omega = 10$–$1600\ {\rm cm}^{-1}$. Here, the imaginary part of the Raman-scattering response χ'' was related to the raw Raman intensity $I_{\rm R}(\omega)$ through the relation $I_R(\omega) = [1 + n(\omega)]\chi''$, where the Bose factor was given by $n(\omega) = [1 - \exp(-\frac{\hbar\omega}{k_B T})]^{-1}$. In Fig. 1(b), $\chi_{\rm dyn}^{(aa)}$ is compared with the static magnetic susceptibility. A close overlap was observed for temperatures down to 70 K. Below this temperature, a discrepancy between the static and dynamic magnetic susceptibilities emerged, indicating a change in the trait of magnetic excitations.

At high temperatures, $T > J$, the magnetism was dictated by $S = 3/2$ spin chains whose dynamic behavior exhibited a dual character of classical and quantum magnetism. For temperatures below J, NNN interactions and interchain couplings became significant, while the competing interactions depleted the spectral weight of lower-energy excitations. This provided a rationale for the anomalies observed in the ESR and Raman data near $T^* \sim J$. Eventually, weak 3D interactions stabilized a weak AFM order at $T_{\rm N}$, while the dynamics remained primarily governed by unconventional spin waves.

IV. CONCLUSIONS

The spin dynamics and low-energy excitations of the $S = 3/2$ spin zigzag chain in the van der Waals material $AgCrP_2S_6$ have been elucidated through ESR and Raman spectroscopy. The characteristics of a low-dimensional spin system in $AgCrP_2S_6$ are evidenced by the development of spin correlations and changes in spin fluctuations observed in the temperature-dependent ESR parameters and magnetic Raman scattering. The salient findings are anomalies at $T^* = 120\,{\rm K}$ in the temperature-dependent ESR parameters, Fano phonon mode, and magnetic contiuum excitations, indicating a change in the nature of the underlying magnetic excitations. Our results suggest that an effective dimension of $AgCrP_2S_6$ is varied due to the competing J_1 and J_2 interactions and interactions between zigzag chains.

ACKNOWLEDGMENTS

This work was supported by the National Research Foundation (NRF) of Korea (Grants No. RS-2023–00209121 and No. 2022R1A2C1003959). R.S. acknowledges the financial support provided by the Ministry of Science and Technology in Taiwan under Projects No. NSTC-111–2124-M-001–009; No. NSTC-110–2112-M-001–065-MY3; and No. AS-iMATE-113–12. Y.C. was supported by the National Research Foundation (NRF) of Korea (Grant No. RS-202300214312).

DATA AVAILABILITY

The data that support the findings of this article are not publicly available. The data are available from the authors upon reasonable request.

[1] P. Aayan, P. Kim, and K. Banerjee, Two-dimensional van der Waals materials, Phys. Today **69**(9), 38 (2016).

[2] Y. Liu, N. O. Weiss, X. Duan, H. -C. Cheng, Y. Huang, and X. Duan, Van der Waals heterostructures and devices, Nat. Rev. Mater. **1**, 16042 (2016).

[3] R. Frisenda, Y. Niu, P. Gant, M. Muñoz, and A. Castellanos-Gomez, Naturally occurring van der Waals materials, npj 2D Mater. Appl. **4**, 38 (2020).

[4] N. Samarth, Magnetism in flatland, Nature (London) **546**, 216 (2017).

[5] J.-G. Park, Opportunities and challenges of 2D magnetic van der Waals materials: Magnetic graphene? J. Phys.: Condens. Matter **28**, 301001 (2016).

[6] R. Roldán, A. Castellanos-Gomez, E. Cappelluti, and F. Guinea, Strain engineering in semiconducting two-dimensional crystals, J. Phys.: Condens. Matter **27**, 313201 (2015).

[7] D. Zhong, K. L. Seyler, X. Linpeng, R. Cheng, N. Sivadas, B. Huang, E. Schmidgall, T. Taniguchi, K. Watanabe, M. A. McGuire, W. Yao, D. Xiao, K.-M. C. Fu, and X. Xu, Van der Waals engineering of ferromagnetic semiconductor

heterostructures for spin and valleytronics, Sci. Adv. **3**, e1603113 (2017).

[8] Y. Cao, V. Fatemi, S. Fang, K. Watanabe, T. Taniguchi, E. Kaxiras, and P. Jarillo-Herrero, Unconventional superconductivity in magic-angle graphene superlattices, Nature (London) **556**, 43 (2018).

[9] M. Buscema, J. O. Island, D. J. Groenendijk, S. I. Blanter, G. A. Steele, H. S. J. van der Zanta, and A. Castellanos-Gomez, Photocurrent generation with two-dimensional van der Waals semiconductors, Chem. Soc. Rev. **44**, 3691 (2015).

[10] W. Zhang, K. He, A. Castellanos-Gomez, and Y. Xie, Van der Waals materials for paper electronics, Trends Chem. **5**, 920 (2023).

[11] S. Conti, L. Pimpolari, G. Calabrese, R. Worsley, S. Majee, D. K. Polyushkin, M. Paur, S. Pace, D. H. Keum, F. Fabbri, G. Iannaccone, M. Macucci, C. Coletti, T. Mueller, C. Casiraghi, and G. Fiori, Low-voltage 2D materials-based printed field-effect transistors for integrated digital and analog electronics on paper, Nat. Commun. **11**, 3566 (2020).

[12] M. Wu, Y. Xiao, Y. Zeng, Y. Zhou, X. Zeng, L. Zhang, and W. Liao, Synthesis of two-dimensional transition metal dichalcogenides for electronics and optoelectronics, InfoMat **3**, 362 (2021).

[13] N. D. Mermin and H. Wagner, Absence of ferromagnetism or antiferromagnetism in one- or two-dimensional isotropic Heisenberg models, Phys. Rev. Lett. **17**, 1133 (1966).

[14] K. S. Burch, D. Mandrus, and J.-G. Park, Magnetism in two-dimensional van der Waals materials, Nature (London) **563**, 47 (2018).

[15] B. Huang, G. Clark, E. Navarro-Moratalla, D. R. Klein, R. Cheng, K. L. Seyler, D. Zhong, E. Schmidgall, M. A. McGuire, D. H. Cobden, W. Yao, D. Xiao, P. Jarillo-Herrero, and X. Xu, Layer-dependent ferromagnetism in a van der Waals crystal down to the monolayer limit, Nature (London) **546**, 270 (2017).

[16] C. Gong, L. Li, Z. Li, H. Ji, A. Stern, Y. Xia, T. Cao, W. Bao, C. Wang, Y. Wang, Z. Q. Qiu, R. J. Cava, S. G. Louie, J. Xia, and X. Zhang, Discovery of intrinsic ferromagnetism in two-dimensional van der Waals crystals, Nature (London) **546**, 265 (2017).

[17] E. Park, J. P. Philbin, H. Chi, J. J. Sanchez, C. Occhialini, G. Varnavides, J. B. Curtis, Z. Song, J. Klein, J. D. Thomsen, M. -G. Han, A. C. Foucher, K. Mosina, D. Kumawat, N. Gonzalez-Yepez, Y. Zhu, Z. Sofer, R. Comin, J. S. Moodera, P. Narang, and F. M. Ross, Anisotropic 2D van der Waals magnets hosting 1D spin chains, Adv. Mater. **36**, 2401534 (2024).

[18] S. Selter, Y. Shemerliuk, B. Büchner, and S. Aswartham, Crystal growth of the quasi-2D quarternary compound $AgCrP_2S_6$ by chemical vapor transport, Crystals **11**, 500 (2021).

[19] J. Sirker, V. Y. Krivnov, D. V. Dmitriev, A. Herzog, O. Janson, S. Nishimoto, S.-L. Drechsler, and J. Richter, $J_1 - J_2$ Heisenberg model at and close to its $Z = 4$ quantum critical point, Phys. Rev. B **84**, 144403 (2011).

[20] K. Okamoto and K. Nomura, Fluid-dimer critical point in $S = 1/2$ antiferromagnetic Heisenberg chain with next nearest neighbor interactions, Phys. Lett. A **169**, 433 (1992).

[21] S. Furukawa, M. Sato, S. Onoda, and A. Furusaki, Ground-state phase diagram of a spin-1/2 frustrated ferromagnetic XXZ chain: Haldane dimer phase and gapped/gapless chiral phases, Phys. Rev. B **86**, 094417 (2012).

[22] J. Igarashi and T. Tonegawa, Excitation spectrum of a spin-1/2 chain with competing interactions, Phys. Rev. B **40**, 756 (1989).

[23] F. Heidrich-Meisner, I. A. Sergienko, A. E. Feiguin, and E. R. Dagotto, Universal emergence of the one-third plateau in the magnetization process of frustrated quantum spin chains, Phys. Rev. B **75**, 064413 (2007).

[24] P. Colombet, A. Leblanc, M. Danot, and J. Rouxel, Coordinance inhabituelle de l'argent dans un sufur lamellaire a sous-reseau magnetique 1D: Le compose $Ag_{0.5}Cr_{0.5}PS_3$, Nouv. J. Chim. **7**, 333 (1983).

[25] C. Payen, H. Mutka, J. L. Soubeyroux, P. Molinié, and P. Colombet, Static and dynamic properties of the quasi-1D Heisenberg antiferromagnets $AgVP_2S_6$ ($S = 1$) and $AgCrP_2S_6$ ($S = 3/2$), J. Magn. Magn. Mater. **104**, 797 (1992).

[26] H. Mutka, J. L. Soubeyroux, G. Bourleaux, and P. Colombet, Support for the Haldane conjecture: Gap for magnetic excitations in the quasi-one-dimensional S = 1 Heisenberg antiferromagnet $AgVP_2S_6$, Phys. Rev. B **39**, 4820 (1989).

[27] H. Mutka, C. Payen, and P. Molinié, One-dimensional Heisenberg antiferromagnet with spin S = 3/2. experiments on $AgCrP_2S_6$, Europhys. Lett. **21**, 623 (1993).

[28] P. W. Anderson and P. R. Weiss, Exchange narrowing in paramagnetic resonance, Rev. Mod. Phys. **25**, 269 (1953).

[29] T. T. P. Cheung, Z. G. Soos, R. E. Dietz, and F. R. Merritt, Temperature dependence of exchange narrowing in the one-dimensional antiferromagnet $N(CH_3)_4MnCl_3$ (TMMC), Phys. Rev. B **17**, 1266 (1978).

[30] H. Tanaka, S. Kuroda, T. Yamashita, M. Mitsumi, and K. Toriumi, ESR studies of the spin dynamics in quasi-one-dimensional iodo-bridged diplatinum complex $Pt_2(n-\text{pentyl}\,CS_2)_4I$, Phys. Rev. B **73**, 245102 (2006).

[31] Y. Oshima, Y. Ishii, F. L. Pratt, I. Watanabe, H. Seo, T. Tsumuraya, T. Miyazaki, and R. Kato, Quasi-one-dimensional spin dynamics in a molecular spin liquid system, Phys. Rev. Lett. **133**, 236702 (2024).

[32] See Supplemental Material at http://link.aps.org/supplemental/10.1103/PhysRevB.111.134415 for the Fano phonon mode deviated from the anharmonic phonon model and for the raw spectra, which include Refs. [33,34].

[33] M. Hong, L. Dai, H. Hu, and C. Li, Structural, ferroelectric, and electronic transitions in the van der Waals multiferroic material $CuCrP_2S_6$ under high temperature and high pressure, Phys. Rev. B **110**, 144103 (2024).

[34] M. Balkanski, R. F. Wallis, and E. Haro, Anharmonic effects in light scattering due to optical phonons in silicon, Phys. Rev. B **28**, 1928 (1983).

[35] J.-H. Lee, S. Lee, Y. Choi, L. Gries, R. Klingeler, K. Raju, R. K. Ulaganathan, R. Sankar, M.-J. Seong, and K.-Y. Choi, Optical probe of magnetic ordering structure and spin-entangled excitons in Mn-substituted $NiPS_3$, Adv. Funct. Mater. **34**, 2405153 (2024).

[36] S. Lee, J. Park, Y. Choi, K. Raju, W.-T. Chen, R. Sankar, and K.-Y. Choi, Chemical tuning of magnetic anisotropy and correlations in $Ni_{1-x}Fe_xPS_3$, Phys. Rev. B **104**, 174412 (2021).

[37] D. Wulferding, Y. Choi, W. Lee, and K.-Y. Choi, Raman spectroscopic diagnostic of quantum spin liquids, J. Phys.: Condens. Matter **32**, 043001 (2020).

[38] M. G. Cottam and D. J. Lockwood, *Light Scattering in Magnetic Solids* (Wiley, New York, 1986).

[39] A. Glamazda, Y. S. Choi, S. -H. Do, S. Lee, P. Lemmens, A. N. Ponomaryov, S. A. Zvyagin, J. Wosnitza, D. P. Sari, I. Watanabe, and K. -Y. Choi, Quantum criticality in the coupled two-leg spin ladder Ba_2CuTeO_6, Phys. Rev. B **95**, 184430 (2017).

[40] Y. Choi, S. Lee, J. -H. Lee, S. Y. Lee, M. -J. Seong, and K. -Y. Choi, Bosonic spinons in anisotropic triangular antiferromagnets, Nat. Commun. **12**, 6453 (2021).

[41] H. Kadowaki, K. Hirakawa, and K. Ubukoshi, Neutron scattering study of magnetic excitations in quasi-one-dimensional triangular lattice antiferromagnet $CsVCl_3$, J. Phys. Soc. Jpn. **52**, 1799 (1983).